Nature of the topological transition of the Kitaev model in [111] magnetic field

S. Thiagarajan,[1] C. Watson,[1] T. Yzeiri,[1,2] H. Hu,[3] B. Uchoa,[4] and F. Krüger[1,2,*]

[1]*London Centre for Nanotechnology, University College London, Gordon St., London WC1H 0AH, United Kingdom*

[2]*ISIS Facility, Rutherford Appleton Laboratory, Chilton, Didcot, Oxfordshire OX11 0QX, United Kingdom*

[3]*School of Physics and Astronomy, University of Birmingham, Edgbaston Park Road, Birmingham B15 2TT, United Kingdom*

[4]*Department of Physics and Astronomy, University of Oklahoma, Norman, Oklahoma 73069, USA*

(Received 16 September 2025; revised 14 January 2026; accepted 20 January 2026; published 5 February 2026)

We investigate the nature of the topological phase transition of the antiferromagnetic Kitaev model on a honeycomb lattice in the presence of a magnetic field along the [111] direction. The field opens a topological gap in the Majorana fermion spectrum and leads to a sequence of topological phase transitions before the field-polarized state is reached. At mean-field level, the gap first closes at the three M points in the Brillouin zone, where the Majorana fermions form Dirac cones, resulting in a change of Chern number by three. An odd number of Dirac fermions in infrared is unusual and requires Berry curvature compensation in ultraviolet, which occurs via topological, ringlike hybridization gaps with higher-energy bands. We perform a renormalization-group analysis of the topological phase transition at the three M points within the Yukawa theory, allowing for intravalley and intervalley fluctuations of the spin-liquid bond operators. We find that the latter lead to a breaking of Lorentz invariance and hence a different universality compared with the standard Ising Gross-Neveu-Yukawa class.

DOI: 10.1103/jjj6-cx8l

I. INTRODUCTION

The celebrated Kitaev honeycomb model, a bond-dependent Ising model, has an exactly solvable quantum spin-liquid (QSL) ground state after the spin-1/2 operators are fractionalized into Majorana fermions [1]. Many efforts to realize this model in materials have utilized spin-orbit coupling, as proposed by Jackeli and Khaliullin [2], for which honeycomb iridates [3–5] and α-$RuCl_3$ [6–8] are promising candidates. However, these materials display long-range zigzag antiferromagnetic (AFM) order at low temperatures [9–11], which can be suppressed in α-$RuCl_3$ by applying a magnetic field [12,13].

These observations have motivated various theoretical and numerical investigations of the AFM Kitaev honeycomb model with an applied field. As already demonstrated in the seminal work by Kitaev [1], in third-order perturbation theory, a small field h along [111] leads to the opening of a topological gap $\Delta \sim h^3$ at the Dirac points with Chern numbers $\mathcal{C} = \pm 1$ of the dispersive Majorana bands. Numerical investigations using exact diagonalization (ED) and density matrix renormalization group (DMRG) reported a $U(1)$ gapless intermediate phase [14–16] sandwiched between the gapped non-Abelian QSL at small fields and the topologically trivial fully polarized phase at large fields. On the other hand, mean-field investigations [17,18] and a variational approach [19] found this intermediate phase to be gapped. It exhibits ringlike low-energy excitations that might be mistaken for a spinor Fermi-surface in numerical studies due to finite-size effects [19]. While DMRG could, in principle, detect gapless modes through the scaling behavior of the entanglement entropy, no convergence was found in the intermediate phase up to the largest system sizes currently accessible [20]. A complementary DMRG study of Kitaev ladders found glassy behavior in the intermediate-field regime due to slow dynamics of Z_2 fluxes [21].

Here, we focus on the first topological transition, between the two gapped QSL phases. At this transition, the total Chern number of the positive bands was found to change from $\mathcal{C}_{\text{tot}} = -1$ in the QSL at small field to $\mathcal{C}_{\text{tot}} = 2$ in the intermediate phase [17–19]. Such a change in Chern number by $\Delta\mathcal{C} = 3$ is consistent with a gap closing at the three M points in the Brillouin zone, as indeed observed in previous mean-field studies [17,18].

The presence of an odd number of Dirac cones at the topological phase transition is unusual and suggests the absence of fermion doubling, as described by the Nielson-Ninomiya theorem [22–25]. To circumvent fermion doubling, it is generically necessary to break at least one of the properties of the Hamiltonian among locality, hermiticity, periodicity, bilinearity, and chiral symmetry. One way is to construct SLAC fermions [26] by introducing long-range hopping terms, which results in a single Dirac cone with singularities at the Brillouin zone boundary [27–30]. Alternatively, one can break the chiral symmetry explicitly [31–34]. For example, in the Bernevig-Hughes-Zhang model [35] and Qi-Wu-Zhang model

*Contact author: f.kruger@ucl.ac.uk

[36], a Wilson term [31] acting like a momentum-dependent mass is applied to obtain a single Dirac cone at zero energy. The other Dirac cone is gapped out and pushed into the ultraviolet (UV) regime. As we will show, the gap closing at the three M points at the field-driven topological phase transition of the Kitaev model is possible because of a UV compensation of Berry curvature due to ringlike hybridization gaps between the low-energy band and higher-energy Majorana fermion modes.

To understand the nature of the topological phase transition, we first briefly revisit the Majorana-fermion parton mean-field theory. Our results are in quantitative agreement with those of earlier mean-field studies [17,18]. In addition, we carefully analyze the role of hybridization gaps and the redistribution of Berry curvature from UV to infrared (IR), thereby providing an understanding of why a gap closing at three M points is possible. We further compute the edge states from an armchair ribbon on the two sides of the topological phase transition. For $h < h_c$, one chiral mode exists on each edge, with chiral central charge of $-1/2$, indicative of non-Abelian anyons and consistent with the total Chern number $\mathcal{C}_{\rm tot} = -1$ for the positive energy bands For $h > h_c$, $\mathcal{C}_{\rm tot} = 2$ corresponds to two chiral Majorana modes per edge, with central charge $+1$. According to Kitaev's 16-fold way [1], the topological order can be described by a chiral $U(1)$ theory with Abelian semion excitations. Therefore, the ground state changes from a gapped Z_2 spin liquid to an Abelian $U(1)$ chiral spin liquid across h_c.

We then use our mean-field results to identify the effective field theory at the topological phase transition around the three M points and perform a renormalization group (RG) calculation within the Gross-Neveu-Yukawa (GNY) approach that is controlled by the number of fermion flavors N. We account for fluctuations of the QSL bond operators for both intravalley and intervalley channels and derive the quantum critical exponents to order $1/N$. We show that intervalley fluctuations explicitly break Lorentz invariance, resulting in a dynamical exponent that departs from $z = 1$. This suggests that the intermediate topological phase transition of the Kitaev QSL at high field is not in the standard Ising GNY universality class.

The paper is organized in the following way: In Sec. II, we describe the AFM Kitaev model on the honeycomb lattice in a magnetic field along [111]. In Sec. III, we perform a nonperturbative mean-field calculation at finite magnetic field and explicitly calculate the Chern numbers of individual bands, the distribution of Berry curvature in the Brillouin zone, and the edge-state spectra in a strip geometry. In Sec. IV, we derive the effective field theory of the topological phase transition and carry out the RG analysis of the transition in the presence of fluctuation fields. We derive the critical exponents and characterize the universality class of the transition. In Sec. V, we summarize our results.

II. MODEL

We consider the AFM Kitaev model on a honeycomb lattice, which is illustrated in Fig. 1(a). The key feature of this model is the bond-directional Ising exchange where, along each of the three different bonds of the honeycomb lattice,

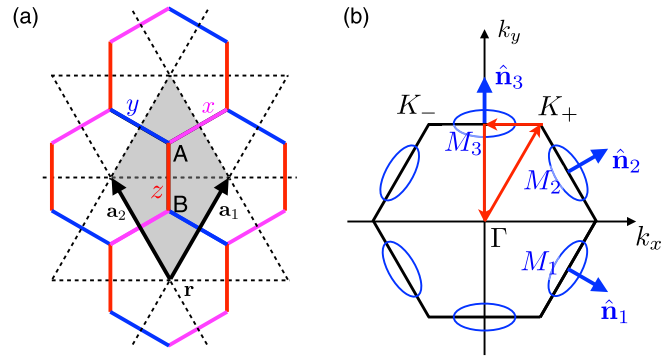

FIG. 1. (a) Illustration of the Kitaev model on a honeycomb lattice. The different bonds are labeled by $\gamma = x, y, z$ and shown in different colors. Along a bond of type γ, only the γ components of the spins are coupled. The unit cell is spanned by the lattice vectors $\mathbf{a}_1$ and $\mathbf{a}_2$ and contains two sites of the honeycomb lattice, labeled A and B. (b) High-symmetry points in the hexagonal Brillouin zone. For small [111] field h, a topological gap $\Delta \sim h^3$ opens at the two K points. At larger field $h = h_c$, we observe a topological phase transition with gap closing at the three M points. The unit vectors $\hat{\mathbf{n}}_i$ parametrize the local coordinate frames at M_i.

labeled by $\gamma = x, y, z$, only the γ components of the spin-1/2 operators are coupled. In addition, the spins are subject to a magnetic field along the [111] direction. The corresponding Hamiltonian can be written as

$$\hat{\mathcal{H}} = \sum_{\mathbf{r},\gamma=x,y,z} \left\{ K\hat{\sigma}_a^\gamma(\mathbf{r})\hat{\sigma}_b^\gamma(\mathbf{r}+\boldsymbol{\delta}_\gamma) - \frac{h}{\sqrt{3}} \sum_{s=a,b} \hat{\sigma}_s^\gamma(\mathbf{r}) \right\}, \quad (1)$$

where $\hat{\sigma}_s^\gamma(\mathbf{r})$ are spin-1/2 operators on the sites $s = a, b$ in the unit cell $\mathbf{r}$ of the triangular lattice spanned by $\mathbf{a}_{1,2} = (\pm\sqrt{3}/2, 3/2)$. Using these conventions, the lattice vectors for the three different bonds are given by $\boldsymbol{\delta}_x = \mathbf{a}_1$, $\boldsymbol{\delta}_y = \mathbf{a}_2$, and $\boldsymbol{\delta}_z = \mathbf{0}$. Measuring the spins in units of $\hbar/2$, the spin commutator relations read $[\hat{\sigma}_s^\alpha(\mathbf{r}), \hat{\sigma}_{s'}^\beta(\mathbf{r}')] = 2\delta_{\mathbf{r},\mathbf{r}'}\delta_{s,s'}\epsilon_{\alpha\beta\gamma}\hat{\sigma}_s^\gamma(\mathbf{r})$.

In the absence of field $h = 0$, the Kitaev model is exactly solvable by expressing the spin operators in terms of a set of four Majorana fermion operators $\hat{\eta}_s^\mu(\mathbf{r})$ ($\mu = 0, x, y, z$),

$$\hat{\sigma}_s^\gamma(\mathbf{r}) = i\hat{\eta}_s^0(\mathbf{r})\hat{\eta}_s^\gamma(\mathbf{r}). \quad (2)$$

The Majorana fermions satisfy the Clifford algebra $\{\hat{\eta}_s^\mu(\mathbf{r}), \hat{\eta}_{s'}^\nu(\mathbf{r}')\} = 2\delta_{\mathbf{r},\mathbf{r}'}\delta_{s,s'}\delta_{\mu,\nu}$ and are subject to the local constraints

$$\hat{\eta}_s^0(\mathbf{r})\hat{\eta}_s^\gamma(\mathbf{r}) + \tfrac{1}{2}\epsilon_{\alpha\beta\gamma}\hat{\eta}_s^\alpha(\mathbf{r})\hat{\eta}_s^\beta(\mathbf{r}) = 0, \quad (3)$$

to correctly represent the spin-Hilbert space.

Although the Kitaev model is quartic in terms of the Majorana fermions, an exact solution can be obtained because the bond operators $\hat{A}_\gamma(\mathbf{r}) = i\hat{\eta}_a^\gamma(\mathbf{r})\hat{\eta}_b^\gamma(\mathbf{r}+\boldsymbol{\delta}_\gamma)$, which have eigenvalues ± 1, are local and commute with the Hamiltonian. As a consequence, it is sufficient to diagonalizr the quadratic Hamiltonian for the $\hat{\eta}^0$ Majorana fermion for a given realization of fluxes, which are obtained by multiplying the corresponding bond operator eigenvalues around each plaquette. In the zero-flux ground-state sector, this results in the energy dispersion $\pm K|1 + \exp(i\mathbf{k}\cdot\mathbf{a}_1) + \exp(i\mathbf{k}\cdot\mathbf{a}_2)|$ for $\hat{\eta}^0$, with Dirac points at the corners $K_\pm$ of the hexagonal Brillouin

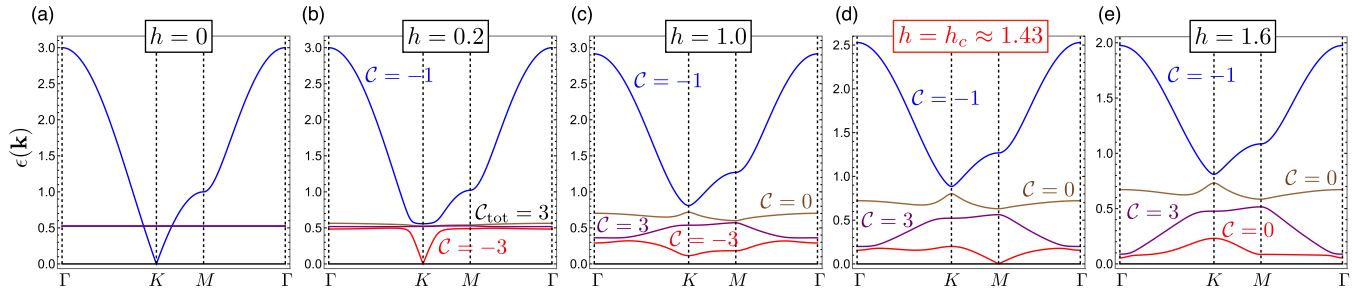

FIG. 2. Evolution of the Majorana fermion mean-field spectrum along a high-symmetry path as a function of magnetic field h along [111]. (a) Spectrum of the Kitaev model at $h = 0$, showing a dispersive Majorana band with Dirac cones at the K points and three degenerate flat bands. (b) For small h, a small gap $\Delta \sim h^3$ open at the K points, and the dispersive band hybridizes with the flat ones. All bands acquire nonzero Chern numbers, where $\mathcal{C} = -3$ for the low-energy band. (c) At $h = 1$, a softening at the M points becomes visible. The Chern numbers remain unchanged. (d) At the critical point $h = h_c \approx 1.43$, the gap closes at the three M points. (e) Bands at $h = 1.6$. The Chern number of the low-energy band changes to $\mathcal{C} = 0$ at $h > h_c \approx 1.43$, indicating the presence of a topological phase transition.

zone [see Fig. 1(b)], and three degenerate flat bands of the local $\hat{\eta}^x$, $\hat{\eta}^y$, and $\hat{\eta}^z$ Majorana fermions, shown in Fig. 2(a).

III. MEAN-FIELD THEORY

A magnetic field along the [111] direction represents the simplest way to break the exact solvability of the Kitaev model. For $h > 0$, the different Majorana fermions hybridize, and the plaquette operators no longer commute with the Hamiltonian. As a first step, we use self-consistent mean-field theory to decouple the quartic Majorana fermion Hamiltonian, introducing the bond expectation values

$$A = \langle i\hat{\eta}_a^\gamma(\mathbf{r})\hat{\eta}_b^\gamma(\mathbf{r}+\boldsymbol{\delta}_\gamma)\rangle,$$
$$B = \langle i\hat{\eta}_a^0(\mathbf{r})\hat{\eta}_b^0(\mathbf{r}+\boldsymbol{\delta}_\gamma)\rangle, \tag{4}$$

which by symmetry take the same values on all nearest-neighbor bonds. To account for effects of internal magnetic fields, we also decouple in the local magnetization channel

$$m_\gamma = \frac{m}{\sqrt{3}} = \langle i\hat{\eta}_s^0(\mathbf{r})\hat{\eta}_s^\gamma(\mathbf{r})\rangle. \tag{5}$$

We treat the three local constraints in Eq. (3) on average through Lagrange multipliers $\lambda_\gamma = \lambda/\sqrt{3}$, with the additional contribution to the Hamiltonian

$$\hat{\mathcal{H}}_\lambda = iK\frac{\lambda}{\sqrt{3}}\sum_{\mathbf{r},s,\gamma}\left\{\hat{\eta}_s^0(\mathbf{r})\hat{\eta}_s^\gamma(\mathbf{r}) + \frac{1}{2}\epsilon_{\alpha\beta\gamma}\hat{\eta}_s^\alpha(\mathbf{r})\hat{\eta}_s^\beta(\mathbf{r})\right\}. \tag{6}$$

In momentum space, the mean-field Hamiltonian has an 8×8 matrix structure ($\mu = 0, x, y, z$ and $s = a, b$). In the following, we measure all energies in units of the Kitaev coupling K. For given mean-field parameters A, B, m and Lagrange parameter λ, we can numerically diagonalize this matrix for each momentum $\mathbf{k}$ in the Brillouin zone, resulting in four pairs of energy eigenvalues $\pm\epsilon_i(\mathbf{k}, A, B, m, \lambda)$, with $\epsilon_i \geqslant 0$, and a zero-temperature mean-field energy per unit cell

$$E = -\sum_{i=1}^{4}\int_{\rm BZ}\frac{d^2\mathbf{k}}{V_{\rm BZ}}\epsilon_i(\mathbf{k}, A, B, m, \lambda) + 3AB + m^2, \tag{7}$$

where $V_{\rm BZ}$ stands for the area of the Brillouin zone. The three equations $\partial E/\partial x = 0$, with $x = A, B, m$, can be conveniently solved using the standard iterative procedure. However, at each iteration step, we need to determine the Lagrange multiplier λ by solving the integral equation $\partial E/\partial\lambda = 0$ with bisection.

A. Mean-field results

For $h = 0$, the mean-field equations can be solved analytically and reproduce the exact solution of the Kitaev model, shown in Fig. 2(a). For small h, a very small gap opens at the K points, which is still barely visible at $h = 0.2$ [see Fig. 2(b)]. In addition, the hybridization between the $\hat{\eta}^0$ and $\hat{\eta}^\gamma$ Majorana fermions results in a ringlike gap feature around the K points. All bands are topologically nontrivial and carry nonzero Chern numbers. Previously, it was demonstrated that the [111] field leads to a topological gap opening of the $\hat{\eta}^0$ Dirac mode in third-order perturbation theory [1]. Ignoring hybridization effects, this then results in Chern numbers $\mathcal{C} = \pm 1$ of the gapped low-energy $\hat{\eta}^0$ mode. While the Chern numbers of all four positive bands still add up to $\mathcal{C}_{\rm tot} = -1$, the formation of hybridization gaps is responsible for a redistribution of Chern numbers between bands, resulting in $\mathcal{C} = -3$ for the low-energy band.

Increasing the field further to $h = 1$, the gap at the K points increases, and a softening of the dispersion at the M points is observed [see Fig. 2(c)]. At the critical field $h_c \approx 1.43$, the gap closes at the three M points, as shown in Fig. 2(d), which have massless Dirac low-energy quasiparticles. As pointed out earlier, an odd number of Dirac points is unusual and only possible if additional Berry curvature is located elsewhere in the Brillouin zone. We address in detail the evolution of the distribution of Berry curvature in the low-energy band in Appendix A.

Beyond the critical field $h > h_c \approx 1.43$, the gap reopens, and the Chern number of the low-energy band changes to $\mathcal{C} = 0$ [see Fig. 2(e)], indicating the presence of a topological phase transition of the low-energy band at $h = h_c$. This results in a total Chern number for the positive energy bands $\mathcal{C}_{\rm tot} = +2$. This critical field value and the total Chern numbers around the phase transition are consistent with values reported in the literature [17,18], noting that, since we measure spins in units of $\hbar/2$, our field values are rescaled by a factor of two. The bond-expectation values A and B, the magnetization m, and the Lagrange multiplier λ evolve smoothly

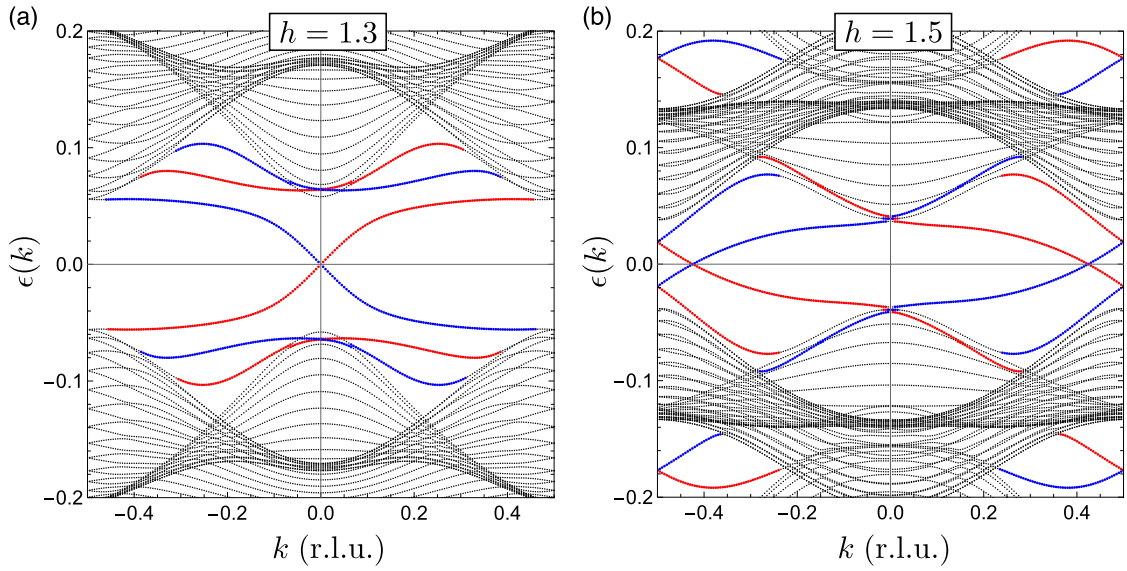

FIG. 3. Edge states calculated from an armchair ribbon at (a) $h = 1.3$ and (b) $h = 1.5$. Bands in blue (red) correspond to the edge states at the left (right) edge. There is one chiral mode per edge for $h < h_c$ and two chiral modes per edge for $h > h_c$, corresponding to the change of total Chern number from -1 to $+2$.

across h_c, suggesting that the transition is purely topological and not associated with a change of symmetry.

The change in total Chern number reflects a change in the number of chiral Majorana edge states due to the bulk-boundary correspondence. The edge modes of an armchair ribbon at $h = 1.3$ and 1.5 are shown in Fig. 3. For $h < h_c$, one chiral mode exists on each edge, with chiral central charge of $-1/2$, indicative of non-Abelian anyons with topological spin $-\pi/8$. For $h > h_c$, the total Chern number $\mathcal{C}_{\text{tot}} = +2$ corresponds to two chiral Majorana modes per edge, with central charge $+1$. According to Kitaev's 16-fold way [1], the topological order can be described by a chiral $U(1)$ theory with Abelian fermion excitations. Therefore, the ground state changes from a gapped Z_2 spin liquid to an Abelian $U(1)$ chiral spin liquid across h_c.

IV. FIELD THEORETICAL ANALYSIS OF TOPOLOGICAL PHASE TRANSITION

A. Effective field theory

At the topological phase transition, the gap closes at the three M points in the Brillouin zone, which we will label by M_i $(i = 1, 2, 3)$ in the following, as illustrated in Fig. 1(b). In a small momentum region around these points and for fields h close to h_c, the low-energy Hamiltonian around M_i will have the conventional 2×2 spinor matrix structure of a gapped Dirac point, where the gap $\Delta \sim (h - h_c)$ is the same at all M points. By symmetry, one would further expect that the Hamiltonians $\hat{\mathcal{H}}_i$ at each M_i are identical when expressed in the local coordinate frame relative to the edge of the Brillouin zone with normal vector $\hat{\mathbf{n}}_i$ (Fig. 1). The Hamiltonian matrices should therefore take the form

$$\mathbf{H}_i(\mathbf{k}) = v_\parallel[(\hat{\mathbf{n}}_i \times \hat{\mathbf{e}}_z) \cdot \mathbf{k}]\boldsymbol{\tau}_x + v_\perp(\hat{\mathbf{n}}_i \cdot \mathbf{k})\boldsymbol{\tau}_y + \Delta\boldsymbol{\tau}_z, \tag{8}$$

where $\boldsymbol{\tau}_\gamma$ are Pauli matrices in pseudospin space. We confirmed this expected form numerically by projecting the full mean-field Hamiltonian onto the low-energy sector, using the set of eigenvectors at each M_i and treating $(h - h_c)$ and the momentum shifts k_x, k_y away from M_i as small perturbations.

Our numerical results show a small anisotropy of Fermi velocities $(v_\parallel - v_\perp)/v_\perp \approx 0.05$. In the following, we will neglect this anisotropy and absorb the velocity $v = v_\parallel = v_\perp$ in a redefinition of $\mathbf{k}$. Our RG analysis will indeed confirm that $v_\parallel = v_\perp$ at the critical fixed point.

The three Dirac Hamiltonians shown in Eq. (8) have the topological charge $\text{sgn}(\Delta)/2$. The additional topological charge of $-3/2$ associated with the nodal line gap around Γ is located at the top of the low-energy band and remains unchanged across the transition. This feature has no direct effect on the nature of the topological phase transition, other than permitting the emergence of an odd number of Dirac cones in the IR via UV compensation. In the following, we focus on the bulk properties in the thermodynamic limit, in the absence of zero-energy edge modes.

Writing the partition function as a Grassmann path integral over Majorana fermion fields, the low-energy free fermion action at the critical point $(\Delta = 0)$ is given by

$$\mathcal{S}_0[\bar{\boldsymbol{\psi}}, \boldsymbol{\psi}] = \sum_{i=1}^{3}\sum_{\nu=1}^{N}\int_{\vec{k}=(k_0,\mathbf{k})} \bar{\boldsymbol{\psi}}_{i\nu}(\vec{k}) \times \{-ik_0 + [(\hat{\mathbf{n}}_i \times \hat{\mathbf{e}}_z) \cdot \mathbf{k}]\boldsymbol{\tau}_x + (\hat{\mathbf{n}}_i \cdot \mathbf{k})\boldsymbol{\tau}_y\}\boldsymbol{\psi}_{i\nu}(\vec{k}), \tag{9}$$

where we have introduced the frequency momentum three-vector $\vec{k} = (k_0, \mathbf{k})$, $i = 1, 2, 3$ labels the three M-point Dirac valleys, and we have generalized to $\nu = 1, \ldots, N$ replicas of the theory, enabling a systematic expansion in $1/(3N)$. The resulting fermion Green function at M_i is given by

$$\mathbf{G}_i(\vec{k}) = \frac{ik_0 + [(\hat{\mathbf{n}}_i \times \hat{\mathbf{e}}_z) \cdot \mathbf{k}]\boldsymbol{\tau}_x + (\hat{\mathbf{n}}_i \cdot \mathbf{k})\boldsymbol{\tau}_y}{\vec{k}^2}. \tag{10}$$

To understand the critical behavior, we need to include fluctuations beyond mean-field theory. The starting point would be a Hubbard-Stratonovich decoupling of the interaction terms in the initial lattice model, which at saddle-point level reproduces the mean-field theory, while the initial fluctuation fields couple to bond operators $i\hat{\eta}^{\gamma}_{a}(\mathbf{r})\hat{\eta}^{\gamma}_{b}(\mathbf{r}+\boldsymbol{\delta}_{\gamma})$ and $i\hat{\eta}^{0}_{a}(\mathbf{r})\hat{\eta}^{0}_{b}(\mathbf{r}+\boldsymbol{\delta}_{\gamma})$, which corresponds to a Yukawa coupling in the sublattice channel $\boldsymbol{\sigma}_{y}$, as discussed in Ref. [37].

To obtain the effective Yukawa couplings in the low-energy field theory, the fermion bond operators need to be transformed to the new basis, using the unitary transformation that diagonalizes the mean-field Hamiltonian at $h = h_c$, followed by a projection onto the low-energy Dirac fermion sector described by the Grassmann fields $\bar{\boldsymbol{\psi}}, \boldsymbol{\psi}$. Since Majorana fermions of different flavors and on different sublattices mix under the unitary transformation, we obtain fluctuations in all channels $\boldsymbol{\tau}_{\gamma}$ of the new low-energy pseudospin space. For simplicity and to reduce the complexity of the consecutive RG analysis, we will focus on the $\boldsymbol{\tau}_{z}$ channel, corresponding to dynamical fluctuations of the mass gap Δ. We stress that the corresponding bosonic fluctuation fields are not related to a physical order parameter. Similar GNY analyses were used in the context of topological phase transitions where two Dirac points merge and a mass gap opens [37,38].

Since the interactions are short ranged, both intervalley and intravalley fluctuations will be important. On the full two-dimensional Brillouin zone, the fluctuations in the mass channel are of the form $\Phi(\mathbf{Q})\bar{\boldsymbol{\psi}}(\mathbf{K})\boldsymbol{\tau}_{z}\boldsymbol{\psi}(\mathbf{K}+\mathbf{Q})$, where we have dropped the dependence on frequencies, for brevity. In the low-energy theory, we only consider momentum patches close to the M points $\mathbf{K} = \mathbf{M}_i + \mathbf{k}$ and define $\boldsymbol{\psi}(\mathbf{K}) = \boldsymbol{\psi}(\mathbf{M}_i + \mathbf{k}) \equiv \boldsymbol{\psi}_i(\mathbf{k})$. For the momentum transfer, we write $\mathbf{Q} = \mathbf{Q}_{ij} + \mathbf{q}$, where $\mathbf{Q}_{ij} = \mathbf{M}_j - \mathbf{M}_i$, and $\mathbf{q}$ is small. Defining the intravalley fluctuation fields ($i = j$) as $\Phi(\mathbf{Q}_{ii} + \mathbf{q}) = \Phi(\mathbf{q}) = \phi(\mathbf{q})$ and the intervalley fluctuation fields ($i \neq j$) as $\Phi(\mathbf{Q}_{ij} + \mathbf{q}) = \varphi_{ij}(\mathbf{q})$, the Yukawa couplings can be written as

$$\mathcal{S}_Y = \frac{g}{\sqrt{3N}} \sum_i \sum_\nu \int_{\vec{k},\vec{q}} \phi(\vec{q}) \bar{\boldsymbol{\psi}}_{i\nu}(\vec{k}) \boldsymbol{\tau}_z \boldsymbol{\psi}_{i\nu}(\vec{k}+\vec{q}) + \frac{\tilde{g}}{\sqrt{6N}} \sum_{i,j}^{i\neq j} \sum_\nu \int_{\vec{k},\vec{q}} \varphi_{ij}(\vec{q}) \bar{\boldsymbol{\psi}}_{i\nu}(\vec{k}) \boldsymbol{\tau}_z \boldsymbol{\psi}_{j\nu}(\vec{k}+\vec{q}), \quad (11)$$

where g and $\tilde{g}$ are the strengths of the intravalley and intervalley Yukawa couplings, respectively. Note that $\varphi^{*}_{ij}(\vec{q}) = \varphi_{ji}(-\vec{q})$. Finally, the quadratic actions for the fluctuation fields are given by

$$\mathcal{S}_0[\phi] = \frac{1}{2} \int_{\vec{q}} D^{-1}(\vec{q}) |\phi(\vec{q})|^2, \quad (12)$$

$$\mathcal{S}_0[\varphi] = \frac{1}{2} \sum_{i,j}^{i<j} \int_{\vec{q}} \tilde{D}^{-1}(\vec{q}) |\varphi_{ij}(\vec{q})|^2, \quad (13)$$

where the inverse boson propagators are given by the usual quadratic gradient and mass terms and a self-energy correction $D^{-1}(\vec{q}) = q_0^2 + c^2\mathbf{q}^2 + m^2 + \Pi(\vec{q})$ and $\tilde{D}^{-1}(\vec{q}) = q_0^2 + \tilde{c}^2\mathbf{q}^2 + \tilde{m}^2 + \tilde{\Pi}(\vec{q})$.

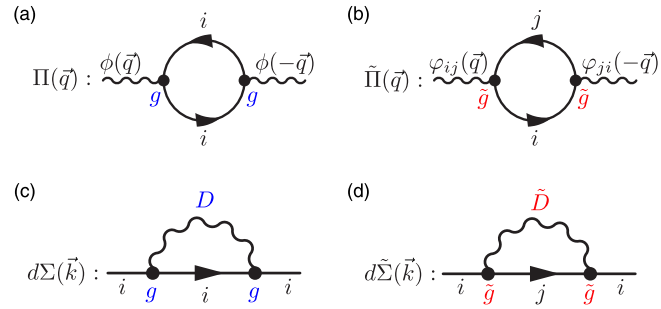

FIG. 4. Self-energy diagrams of the GNY model. Top row: Bosonic self-energy diagrams. Fermionic polarization bubble diagrams give nonanalytic IR corrections to boson propagators of (a) intravalley and (b) intervalley fluctuation fields ($i \neq j$). Bottom row: Fermionic self-energy corrections, leading to a renormalization of the free fermion action. (c) shows the contribution $d\Sigma(\vec{k})$ from intravalley fluctuations and (d) the contribution $d\tilde{\Sigma}(\vec{k})$ from fluctuations between different valleys, $i \neq j$.

B. Self-energy corrections and IR boson propagators

The self-energy corrections to the boson propagators correspond to the diagrams shown in Figs. 4(a) and 4(b) and are given by $\Pi(\vec{q}) = g^2[f_{ii}(\vec{q}) - f_{ii}(\vec{0})]$ and $\tilde{\Pi}(\vec{q}) = \frac{\tilde{g}^2}{3}[f_{ij}(\vec{q}) - f_{ij}(\vec{0})]$ for $i \neq j$, where

$$f_{ij}(\vec{q}) = \int_{\vec{k}} \mathrm{Tr}\{\mathbf{G}_i(\vec{k})\boldsymbol{\tau}_z\mathbf{G}_j(\vec{k}+\vec{q})\boldsymbol{\tau}_z\}. \quad (14)$$

The polarization diagrams can be computed analytically, see Appendix B, resulting in

$$f_{ij}(\vec{q}) - f_{ij}(\vec{0}) = \frac{2(1+\cos\beta_{ij})q_0^2 + (1+3\cos\beta_{ij})\mathbf{q}^2}{32|\vec{q}|}, \quad (15)$$

where β_{ij} is the angle between the unit vectors $\hat{\mathbf{n}}_i$ and $\hat{\mathbf{n}}_j$ at valleys M_i and M_j, $\cos\beta_{ij} = \hat{\mathbf{n}}_i \cdot \hat{\mathbf{n}}_j$. Using $\cos\beta_{ij} = 1$ for the intravalley ($i = j$) and $\cos\beta_{ij} = \cos(\pm\pi/3) = 1/2$ for the intervalley terms ($i \neq j$), we obtain the boson self-energy corrections

$$\Pi(\vec{q}) = \frac{g^2}{8}|\vec{q}|, \quad (16)$$

$$\tilde{\Pi}(\vec{q}) = \frac{\tilde{g}^2}{32}|\vec{q}|\left(1 - \frac{1}{6}\frac{\mathbf{q}^2}{\vec{q}^2}\right), \quad (17)$$

for intravalley and intervalley fluctuation channels, respectively. The intravalley correction in Eq. (16) is the standard result, as shown in Ref. [39].

The self-energy corrections of both channels scale as $\sim|\vec{q}| = \sqrt{q_0^2 + \mathbf{q}^2}$ and hence dominate over the conventional quadratic gradient terms in the IR limit. To understand the universality of the transition, it is sufficient to keep the leading frequency and momentum dependence and use $D^{-1}(\vec{q}) = \Pi(\vec{q})$ and $\tilde{D}^{-1}(\vec{q}) = \tilde{\Pi}(\vec{q})$ as inverse IR propagators.

C. RG analysis

We proceed to analyze the GNY action $\mathcal{S}_0[\bar{\boldsymbol{\psi}}, \boldsymbol{\psi}] + \mathcal{S}_0[\phi] + \mathcal{S}_0[\varphi] + \mathcal{S}_Y[\bar{\boldsymbol{\psi}}, \boldsymbol{\psi}, \phi, \varphi]$ using a RG approach. Since

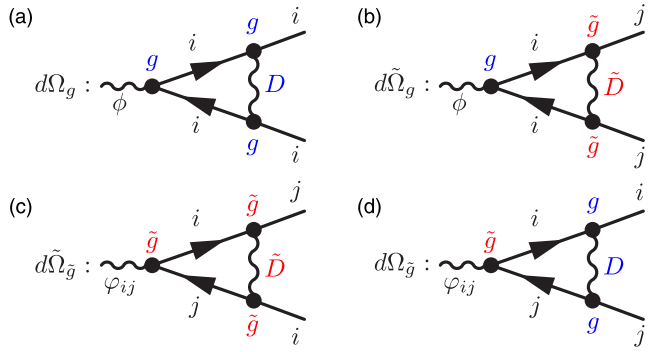

FIG. 5. Diagrams that renormalize (a) and (b) the intravalley Yukawa coupling g and (c) and (d) the Yukawa coupling $\tilde{g}$ between different valleys $i \neq j$.

our aim is to understand the effects of critical intravalley and intervalley fluctuations at $\Delta = 0$ ($h = h_c$), the different band topologies on the two sides of the quantum phase transition are not relevant to the following analysis.

We integrate out UV modes from the infinitesimal three-dimensional frequency-momentum shell

$$\Lambda \exp(-d\ell) \leqslant |\vec{k}| \leqslant \Lambda, \tag{18}$$

where Λ denotes the original cutoff of the theory. The diagrams that renormalize the free fermion action and Yukawa couplings are shown in Fig. 4 (bottom row) and Fig. 5, respectively. Note that the IR boson propagators are nonanalytic and do not renormalize under the perturbative shell RG scheme. The shell integration is followed by a rescaling of frequency and momentum

$$k_0 \to k_0 \exp(-zd\ell), \quad \mathbf{k} \to \mathbf{k} \exp(-d\ell), \tag{19}$$

and fields

$$\begin{aligned} \boldsymbol{\psi} &\to \boldsymbol{\psi} \exp(-\Delta_{\boldsymbol{\psi}}/2\, d\ell), \quad \phi \\ &\to \phi \exp(-\Delta_{\phi}/2\, d\ell), \quad \varphi \to \varphi \exp(-\Delta_{\varphi}/2\, d\ell). \end{aligned} \tag{20}$$

We start by analyzing the shell corrections to the free fermion action, corresponding to the diagrams in Figs. 4(c) and 4(d), and given by

$$d\mathcal{S}_0[\bar{\boldsymbol{\psi}}, \boldsymbol{\psi}] = \sum_{i,\nu} \int_{\vec{k}}^{<} \bar{\boldsymbol{\psi}}_{i\nu}(\vec{k})[d\boldsymbol{\Sigma}_i(\vec{k}) + d\tilde{\boldsymbol{\Sigma}}_i(\vec{k})]\boldsymbol{\psi}_{i\nu}(\vec{k}), \tag{21}$$

with

$$d\boldsymbol{\Sigma}_i(\vec{k}) = -\frac{g^2}{3N} \int_{\vec{q}}^{>} D(\vec{q})\boldsymbol{\tau}_z \mathbf{G}_i(\vec{k}+\vec{q})\boldsymbol{\tau}_z, \tag{22}$$

$$d\tilde{\boldsymbol{\Sigma}}_i(\vec{k}) = -\frac{\tilde{g}^2}{6N} \sum_{j(\neq i)} \int_{\vec{q}}^{>} \tilde{D}(\vec{q})\boldsymbol{\tau}_z \mathbf{G}_j(\vec{k}+\vec{q})\boldsymbol{\tau}_z, \tag{23}$$

for the infinitesimal intravalley and intervalley fermion self-energy corrections. In the above and the following, $>$ denotes integration over the infinitesimal shell in Eq. (18), $<$ over modes up to the reduced cutoff $|\vec{k}| \leqslant \Lambda \exp(-d\ell)$.

Expanding Eqs. (22) and (23) to linear order in outer frequency k_0 and momenta $\mathbf{k}$,

$$\begin{aligned} d\boldsymbol{\Sigma}_i(\vec{k}) + d\tilde{\boldsymbol{\Sigma}}_i(\vec{k}) = &-ik_0(\Sigma_0 + \tilde{\Sigma}_0)d\ell \\ &+ [(\hat{\mathbf{n}}_i \times \hat{\mathbf{e}}_z)\cdot \mathbf{k}]\boldsymbol{\tau}_x(\Sigma_x + \tilde{\Sigma}_x)d\ell \\ &+ (\hat{\mathbf{n}}_i \cdot \mathbf{k})\boldsymbol{\tau}_y(\Sigma_y + \tilde{\Sigma}_y)d\ell, \end{aligned} \tag{24}$$

and carrying out the resulting shell integrals over $\vec{q}$ for the coefficients $\Sigma_n d\ell$ and $\tilde{\Sigma}_n d\ell$ ($n = 0, x, y$), we obtain

$$\Sigma_0 = \Sigma_x = \Sigma_y = \frac{1}{3N}\frac{4}{3\pi^2}, \tag{25}$$

for the intravalley contributions and

$$\tilde{\Sigma}_0 = \frac{1}{3N}\frac{96(11\kappa - 2)}{\pi^2}, \quad \tilde{\Sigma}_{x,y} = \frac{1}{3N}\frac{48(1-5\kappa)}{\pi^2}, \tag{26}$$

for the intervalley terms, where we have defined $\kappa = (1/\sqrt{5})\arctan(1/\sqrt{5})$. Details of the calculation can be found in Appendix C. Combining the loop corrections with the rescaling contributions and demanding that the inverse fermion propagator remains invariant under RG, we obtain the conditions

$$-2 - 2z - \Delta_{\psi} + \Sigma_0 + \tilde{\Sigma}_0 = 0, \tag{27}$$

$$-3 - z - \Delta_{\psi} + \Sigma_{x,y} + \tilde{\Sigma}_{x,y} = 0, \tag{28}$$

from the scale invariance of the frequency and spatial momentum coefficients, respectively. These equations allow us to determine the dynamical exponent

$$\begin{aligned} z &= 1 + \tilde{\Sigma}_0 - \tilde{\Sigma}_{x,y} \\ &= 1 + \frac{1}{3N}\frac{48(27\kappa - 5)}{\pi^2} \approx 1 + \frac{0.379}{3N}, \end{aligned} \tag{29}$$

and the fermion anomalous dimension

$$\begin{aligned} \eta_{\psi} &= \Sigma_0 - \tilde{\Sigma}_0 + 2\tilde{\Sigma}_{x,y} \\ &= \frac{1}{3N}\frac{4(217 - 1152\kappa)}{3\pi^2} \approx \frac{0.047}{3N}, \end{aligned} \tag{30}$$

which measures the deviation of Δ_{ψ} from tree-level scaling $\Delta_{\psi} = -4 + \eta_{\psi}$.

Finally, we compute the renormalization of the Yukawa couplings g and $\tilde{g}$. The corresponding one-loop diagrams involve contractions of three Yukawa vertices and are shown in Fig. 5. Note that, since $g^2 D(\vec{q}) \sim g^0$ and $\tilde{g}^2\tilde{D}(\vec{q}) \sim \tilde{g}^0$, the RG equations for g and $\tilde{g}$ decouple and take the simple linear form

$$\frac{dg}{d\ell} = \left(-4 - 2z - \Delta_{\psi} - \frac{\Delta_{\phi}}{2} + \Omega_g + \tilde{\Omega}_g\right)g, \tag{31}$$

$$\frac{d\tilde{g}}{d\ell} = \left(-4 - 2z - \Delta_{\psi} - \frac{\Delta_{\varphi}}{2} + \Omega_{\tilde{g}} + \tilde{\Omega}_{\tilde{g}}\right)\tilde{g}, \tag{32}$$

where we have included the rescaling contributions. The one-loop corrections $d\Omega_g = \Omega_g d\ell$ and $d\tilde{\Omega}_g = \tilde{\Omega}_g d\ell$ that contribute to the renormalization of the intravalley coupling g are

given by the shell integrals

$$\Omega_g d\ell = \frac{g^2}{3N}\int_{\vec{q}}^{>} D(\vec{q})\mathbf{G}_i(\vec{q})\boldsymbol{\tau}_z\mathbf{G}_i(\vec{q})\boldsymbol{\tau}_z = -\frac{d\ell}{3N}\frac{4}{\pi^2}, \quad (33)$$

$$\tilde{\Omega}_g d\ell = \frac{\tilde{g}^2}{3N}\int_{\vec{q}}^{>} \tilde{D}(\vec{q})\mathbf{G}_i(\vec{q})\boldsymbol{\tau}_z\mathbf{G}_i(\vec{q})\boldsymbol{\tau}_z = -\frac{d\ell}{3N}\frac{96\kappa}{\pi^2}, \quad (34)$$

which correspond to the diagrams in Figs. 5(a) and 5(b). In the same way, the diagrammatic contributions that contribute to the renormalization of the intervalley Yukawa coupling $\tilde{g}$ are given by

$$\Omega_{\tilde{g}} d\ell = \frac{g^2}{3N}\int_{\vec{q}}^{>} D(\vec{q})\mathbf{G}_i(\vec{q})\boldsymbol{\tau}_z\mathbf{G}_j(\vec{q})\boldsymbol{\tau}_z = -\frac{d\ell}{3N}\frac{8}{3\pi^2}, \quad (35)$$

$$\tilde{\Omega}_{\tilde{g}} d\ell = \frac{\tilde{g}^2}{6N}\int_{\vec{q}}^{>} \tilde{D}(\vec{q})\mathbf{G}_i(\vec{q})\boldsymbol{\tau}_z\mathbf{G}_j(\vec{q})\boldsymbol{\tau}_z = -\frac{d\ell}{3N}\frac{24(1-4\kappa)}{\pi^2}, \quad (36)$$

and correspond to the diagrams in Figs. 5(c) and 5(d). Detail on the calculation of the above one-loop diagrams can be found in Appendix D.

Since it is possible to scale g and $\tilde{g}$ out of the large-N IR theory by a simple rescaling of the fluctuation fields $g\phi \to \phi$ and $\tilde{g}\varphi_{ij} \to \varphi_{ij}$, we need to postulate that both Yukawa couplings are scale invariant $\frac{dg}{d\ell} = \frac{d\tilde{g}}{d\ell} = 0$. From Eqs. (31) and (32) and using our results for z and Δ_ψ, we obtain the scaling dimensions $\Delta_\phi = -4 + \eta_\phi$ and $\Delta_\varphi = -4 + \eta_\varphi$ of the fluctuation fields, where their resulting anomalous dimensions are

$$\eta_\phi = 2\left(\Omega_g + \tilde{\Omega}_g - \Sigma_0 - \tilde{\Sigma}_0\right) = -\frac{1}{3N}\frac{32(216\kappa - 35)}{3\pi^2} \approx -\frac{6.077}{3N}, \quad (37)$$

$$\eta_\varphi = 2\left(\Omega_{\tilde{g}} + \tilde{\Omega}_{\tilde{g}} - \Sigma_0 - \tilde{\Sigma}_0\right) = -\frac{1}{3N}\frac{8(240\kappa - 41)}{\pi^2} \approx -\frac{3.353}{3N}. \quad (38)$$

To summarize, we have obtained the dynamical critical exponent z in Eq. (29), the fermion anomalous dimension η_ψ in Eq. (30), and the anomalous dimensions η_ϕ in Eq. (37) and η_φ in Eq. (38) of the intravalley and intervalley fluctuation fields at one-loop order, which systematically accounts for contributions of order $1/(3N)$. At the topological phase transition, the mass gap of the $3N$ Dirac fermions closes, and we considered a GNY theory where both the dynamical intravalley and intervalley mass fluctuations are critical.

Let us compare with the case where the intervalley fluctuations are absent $\tilde{g} = 0$. This would simply mean that the intervalley fluctuations are gapped and short ranged. One would therefore expect to see a crossover from the universal behavior with the set of critical exponents computed above to the universality of a GNY theory with $\tilde{g} = 0$. We can obtain the critical exponents without intervalley coupling by setting $\tilde{\Sigma}_0 = \tilde{\Sigma}_{x,y} = \Omega_{\tilde{g}} = \tilde{\Omega}_g = \tilde{\Omega}_{\tilde{g}} = 0$, resulting in

$$z = 1, \quad \eta_\psi = \frac{1}{3N}\frac{4}{3\pi^2}, \quad \eta_\phi = -\frac{1}{3N}\frac{32}{3\pi^2}, \quad (39)$$

which are the known critical exponents of the Ising-GNY theory in $2+1$ dimensions in the limit of a large number of decoupled $3N$ copies of two-component Dirac fermion fields [40–43].

The comparison shows that the presence of critical or at least very soft intervalley fluctuations has important consequences for the universal critical behavior. Most importantly, it leads to a breaking of Lorentz invariance ($z > 1$). While the changes of the fermion anomalous dimension are small, the anomalous dimensions of the bosonic fluctuation fields are significantly larger than that of the conventional GNY theory.

We reiterate that we only considered fluctuations in the mass channel $\boldsymbol{\tau}_z$, for simplicity. The additional fluctuations in other channels, e.g., in the bond channel $\boldsymbol{\tau}_y$, can be analyzed in a completely analogous way, and they would give additional contributions to the anomalous dimensions η_ψ and η_ϕ as well as to the dynamical exponent z if such fluctuations are between valleys. However, the main conclusion of our analysis that intervalley fluctuations break Lorentz invariance will still hold.

V. DISCUSSION

In conclusion, we have addressed the nature of the field-driven topological phase transition of the Kitaev QSL. Our mean-field results clarify the closing of the low-energy band gap of the intermediate phase at the three M points in the Brillouin zone and the necessity to incorporate the hybridization with the high-energy bands to account for the absence of fermion doubling in the IR, which is manifested through the presence of an odd number of Dirac cones. The hybridization makes the high-energy bands topological while permitting a redistribution of Berry curvature from UV to IR.

We then performed a Wilson momentum shell RG calculation in the GNY model to describe the nature of the quantum phase transition beyond mean field. We showed that the intervalley fluctuation channel among different M points breaks Lorentz invariance and produces a dynamical exponent $z > 1$. Intervalley fluctuations produce small corrections to the mean-field critical exponents, with the exception of the anomalous dimension of the bosonic fields, where the effect is significant. The conclusion is that the intermediate topological phase transition of the Kitaev QSL at finite [111] field belongs to a different universality class than the standard Ising GNY one.

ACKNOWLEDGMENTS

We acknowledge Arnaud Ralko for helpful discussions. B.U. acknowledges NSF Grant No. DMR-2529526 for support.

DATA AVAILABILITY

No data were created or analyzed in this study.

APPENDIX A: LOW-ENERGY BAND BERRY CURVATURE

In Fig. 6 we analyze the evolution of the low-energy band Berry curvature $\Omega(\mathbf{k})$ for different field values. At very small field, $h = 0.006$ [see Fig. 6(a)], we find negative spikes with

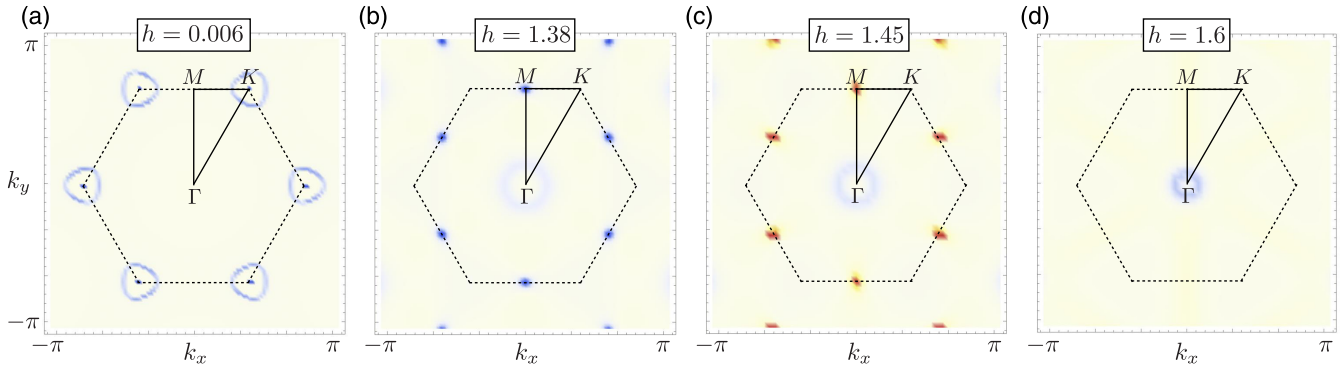

FIG. 6. Berry curvature $\Omega(\mathbf{k})$ of the low-energy band for different values of magnetic field. (a) At small field ($h = 0.006$) negative Berry curvature is concentrated at each K point as well as around the nodal line gap around K from hybridization with the flat bands. (b) and (c) show the change of topological charge at the M points from $-1/2$ to $1/2$ across the topological phase transition. The missing Berry curvature of $-3/2$ is concentrated at a nodal line gap around Γ. (d) At $h = 1.6$ Berry curvature is delocalized along the Γ-M high-symmetry directions and the nodal-line gap around Γ starts to contract.

topological charge of $-1/2$ at the K points, as expected. In addition, there is a ring-like feature in the UV with $\Omega(\mathbf{k}) < 0$ around each K point. This feature coincides with the hybridization gap forming at the intersection line between the Dirac mode and the flat bands, see Fig. 2. Each ring constitutes a topological charge of -1, resulting in a Chern number of $\mathcal{C} = 2 \times (-1/2) + 2 \times (-1) = -3$ of the low-energy band.

Figures 6(b) and 6(c) show the Berry curvature $\Omega(\mathbf{k})$ at fields slightly below ($h = 1.38$) and above ($h = 1.45$) the critical value $h_c \approx 1.43$, where there is a topological phase transition. As anticipated, the topological charge changes from $-1/2$ to $+1/2$ at each M point, resulting in a Chern number change $\Delta\mathcal{C} = 3$ across the transition. The missing Berry curvature of $-3/2$ is centered around a nodal line gap around Γ between the low-energy and first exited bands. This nodal line gap remains intact across the transition and is clearly visible in the spectrum at h_c, shown in Fig. 2(d). Increasing the field to $h = 1.6$ [see Fig. 6(d)], the topological charge from the M points seems to delocalise along the Γ-M high-symmetry lines, along which the low-energy dispersion is practically flat [see Fig. 2(e)]. Moreover, the nodal line gap around Γ seems to contract and move to lower energies.

Since the ground state remains topological at $h = 1.6$, there needs to be at least one additional topological phase transition before the topologically trivial field polarized state is obtained at large h. Unfortunately, the numerics becomes unstable in this field range, which might be in part due to the confinement of Majorana fermions, which is not captured in the mean-field treatment.

APPENDIX B: BOSONIC SELF-ENERGY CORRECTIONS

We will evaluate the regularized polarization bubble diagram $f_{ij}(\vec{q}) - f_{ij}(\vec{0})$ defined in Eq. (14). Inserting the expressions for the fermion Green function (10), using that $\boldsymbol{\tau}_z^2 = 1$, $\boldsymbol{\tau}_z\boldsymbol{\tau}_x\boldsymbol{\tau}_z = -\boldsymbol{\tau}_x$, and $\boldsymbol{\tau}_z\boldsymbol{\tau}_y\boldsymbol{\tau}_z = -\boldsymbol{\tau}_y$ and taking the trace over pseudo-spin space, using that $\mathrm{Tr}(\boldsymbol{\tau}_\alpha\boldsymbol{\tau}_\beta) = 2\delta_{\alpha\beta}$, we obtain

$$f_{ij}(\vec{q}) = -2\int_{\vec{k}} \frac{F_{ij}(\vec{k},\vec{q})}{\vec{k}^2(\vec{k}+\vec{q})^2}, \tag{B1}$$

where

$$F_{ij}(\vec{k},\vec{q}) = k_0(k_0+q_0) + \cos\beta_{ij}\mathbf{k}(\mathbf{k}+\mathbf{q}) - \sin\beta_{ij}(k_x q_y - k_y q_x). \tag{B2}$$

Here, β_{ij} denotes the angle between the unit vectors $\hat{\mathbf{n}}_i$ and $\hat{\mathbf{n}}_j$. Subtracting

$$f_{ij}(\vec{0}) = -2\int_{\vec{k}} \frac{k_0^2 + \cos\beta_{ij}\mathbf{k}^2}{\vec{k}^4} = -\frac{2}{3}\int_{\vec{k}} \frac{1+2\cos\beta_{ij}}{\vec{k}^2} \tag{B3}$$

results in

$$\tilde{f}_{ij}(\vec{q}) = f_{ij}(\vec{q}) - f_{ij}(\vec{0}) = 2\int_{\vec{k}} \frac{\tilde{F}_{ij}(\vec{k},\vec{q})}{\vec{k}^2(\vec{k}+\vec{q})^2}, \tag{B4}$$

with $\tilde{F}_{ij}(\vec{k},\vec{q}) = \frac{1}{3}(1+2\cos\beta_{ij})(\vec{k}+\vec{q})^2 - F_{ij}(\vec{k},\vec{q})$. The IR behavior of $\tilde{f}_{ij}(\vec{q})$ is dominated by the small $\vec{k}$ contributions to the integral. We can therefore send the UV cut-off to infinity, what enables us to use the standard Feynman parametrization trick.

We first introduce a dummy integration variable using the formula $1/(ab) = \int_0^1 dt/[ta + (1-t)b]^2$ with $a = (\vec{k}+\vec{q})^2$ and $b = \vec{k}^2$, followed by a shift of the frequency-momentum vector, $\vec{p} = \vec{k} + t\vec{q}$, to obtain

$$\tilde{f}_{ij}(\vec{q}) = 2\int_0^1 dt \int_{\vec{p}} \frac{\tilde{F}_{ij}(\vec{p}-t\vec{q},\vec{q})}{[\vec{p}^2 + t(1-t)\vec{q}^2]^2}. \tag{B5}$$

The denominator is now rotationally symmetric in $\vec{p}$ and, as a result, the terms in $\tilde{F}_{ij}(\vec{p}-t\vec{q},\vec{q})$ that are linear in $\vec{p}$ vanish under integration. Moreover, the terms that are quadratic in the components of $\vec{p}$ cancel each other under integration, leaving

the remaining integral

$$\tilde{f}_{ij}(\vec{q}) = 2\int_0^1 dt\Big\{(1-t)^2\frac{1+2\cos\beta_{ij}}{3}\vec{q}^2 + t(1-t)\big(q_0^2+\cos\beta_{ij}\mathbf{q}^2\big)\Big\}\int_{\vec{p}}\frac{1}{[\vec{p}^2+t(1-t)\vec{q}^2]^2}. \tag{B6}$$

After carrying out the radially symmetric, three dimensional $\vec{p}$ integral we obtain

$$\tilde{f}_{ij}(\vec{q}) = \frac{1}{4\pi|\vec{q}|}\int_0^1\frac{dt}{\sqrt{t(1-t)}}\Big\{(1-t)^2\frac{1+2\cos\beta_{ij}}{3}\vec{q}^2 + t(1-t)(q_0^2+\cos\beta_{ij}\mathbf{q}^2)\Big\}. \tag{B7}$$

The integrals over t are elementary,

$$\int_0^1 dt\frac{(1-t)^2}{\sqrt{t(1-t)}} = \frac{3\pi}{8} \quad\text{and}\quad \int_0^1 dt\frac{t(1-t)}{\sqrt{t(1-t)}} = \frac{\pi}{8}, \tag{B8}$$

resulting in Eq. (15).

APPENDIX C: FERMION SELF ENERGY CORRECTIONS

Let us first evaluate the fermion self energy correction $d\boldsymbol{\Sigma}_i(\vec{k})$ in Eq. (22) from the intra-valley fluctuations. After Taylor expansion in external frequencies and momenta to linear order, the coefficients $\Sigma_n d\ell$ in Eq. (24) are obtained as the following shell integrals,

$$\Sigma_0 d\ell = \frac{g^2}{3N}\int_{\vec{q}}^{>}\frac{D(\vec{q})}{\vec{q}^2}\left(1-2\frac{q_0^2}{\vec{q}^2}\right) \tag{C1}$$

$$\Sigma_x d\ell = \frac{g^2}{3N}\int_{\vec{q}}^{>}\frac{D(\vec{q})}{\vec{q}^2}\left(1-2\frac{[(\hat{\mathbf{n}}_i\times\hat{\mathbf{e}}_z)\cdot\mathbf{q}]^2}{\vec{q}^2}\right) \tag{C2}$$

$$\Sigma_y d\ell = \frac{g^2}{3N}\int_{\vec{q}}^{>}\frac{D(\vec{q})}{\vec{q}^2}\left(1-2\frac{(\hat{\mathbf{n}}_i\cdot\mathbf{q})^2}{\vec{q}^2}\right). \tag{C3}$$

Since $D(\vec{q})$ is rotationally symmetric it follows that $\Sigma_0 = \Sigma_x = \Sigma_y$ and

$$\Sigma_n d\ell = \frac{g^2}{3N}\int_{\vec{q}}^{>}\frac{D(\vec{q})}{\vec{q}^2}\times\left(1-\frac{2}{3}\right) = \frac{1}{3N}\frac{8}{3}\int_{\vec{q}}^{>}\frac{1}{|\vec{q}|^3} = \frac{1}{3N}\frac{4}{3\pi^2}\int_{\Lambda e^{-d\ell}}^{\Lambda}\frac{dq}{q} = \frac{1}{3N}\frac{4}{3\pi^2}d\ell. \tag{C4}$$

In the case of the inter-valley contributions an additional complication arises from the fact that $d\tilde{\boldsymbol{\Sigma}}_i(\vec{k})$ in Eq. (23) involves a sum over Green functions $\mathbf{G}_j$ from neighboring valleys. However, using that $\sum_{j(\neq i)}\hat{\mathbf{n}}_j = \hat{\mathbf{n}}_i$ we obtain

$$-\sum_{j(\neq i)}\boldsymbol{\tau}_z\mathbf{G}_j(\vec{k}+\vec{q})\boldsymbol{\tau}_z = \frac{-2i(k_0+q_0)+(\hat{\mathbf{n}}_i\times\hat{\mathbf{e}}_z)\cdot(\mathbf{k}+\mathbf{q})\boldsymbol{\tau}_x+\hat{\mathbf{n}}_i\cdot(\mathbf{k}+\mathbf{q})\boldsymbol{\tau}_y}{(\vec{k}+\vec{q})^2}. \tag{C5}$$

Proceeding with the Taylor expansion as in the intravalley case, this results in

$$\tilde{\Sigma}_0 d\ell = \frac{\tilde{g}^2}{3N}\int_{\vec{q}}^{>}\frac{\tilde{D}(\vec{q})}{\vec{q}^2}\left(1-2\frac{q_0^2}{\vec{q}^2}\right) \tag{C6}$$

$$\tilde{\Sigma}_x d\ell = \frac{\tilde{g}^2}{6N}\int_{\vec{q}}^{>}\frac{\tilde{D}(\vec{q})}{\vec{q}^2}\left(1-2\frac{[(\hat{\mathbf{n}}_i\times\hat{\mathbf{e}}_z)\cdot\mathbf{q}]^2}{\vec{q}^2}\right) \tag{C7}$$

$$\tilde{\Sigma}_y d\ell = \frac{\tilde{g}^2}{6N}\int_{\vec{q}}^{>}\frac{\tilde{D}(\vec{q})}{\vec{q}^2}\left(1-2\frac{(\hat{\mathbf{n}}_i\cdot\mathbf{q})^2}{\vec{q}^2}\right). \tag{C8}$$

Inserting $\tilde{D}(\vec{q})$ and using spherical coordinates we obtain

$$\begin{aligned}\tilde{\Sigma}_0 d\ell &= \frac{32}{3N}\int_{\vec{q}}^{>}\frac{1}{|\vec{q}|^3}\frac{1-2\frac{q_0^2}{\vec{q}^2}}{1-\frac{1}{6}\frac{\mathbf{q}^2}{\vec{q}^2}}\\ &= \frac{1}{3N}\frac{8}{\pi^2}d\ell\int_0^\pi d\theta\sin\theta\frac{1-2\cos^2\theta}{1-\frac{1}{6}\sin^2\theta}\\ &= \frac{1}{3N}\frac{96}{\pi^2}\left[\frac{11}{\sqrt{5}}\arctan\left(\frac{1}{\sqrt{5}}\right)-2\right]d\ell \qquad\text{(C9)}\\ &= \frac{1}{3N}\frac{96(11\kappa-2)}{\pi^2}d\ell \qquad\text{(C10)}\end{aligned}$$

for the frequency coefficient, where we have defined

$$\kappa = \frac{1}{\sqrt{5}}\arctan\left(\frac{1}{\sqrt{5}}\right). \tag{C11}$$

Likewise, for the coefficients of the spatial momentum terms we obtain

$$\begin{aligned}\tilde{\Sigma}_{x,y} d\ell &= \frac{32}{6N}\int_{\vec{q}}^{>}\frac{1}{|\vec{q}|^3}\frac{1-\frac{\mathbf{q}^2}{\vec{q}^2}}{1-\frac{1}{6}\frac{\mathbf{q}^2}{\vec{q}^2}}\\ &= \frac{1}{3N}\frac{4}{\pi^2}d\ell\int_0^\pi d\theta\sin\theta\frac{1-\sin^2\theta}{1-\frac{1}{6}\sin^2\theta}\\ &= \frac{1}{3N}\frac{48(1-5\kappa)}{\pi^2}d\ell. \qquad\text{(C12)}\end{aligned}$$

APPENDIX D: CORRECTIONS TO YUKAWA COUPLINGS

The loop corrections to the Yukawa couplings can be written as $\Omega_g d\ell = \frac{1}{3N}g_{ii}d\ell$, $\tilde{\Omega}_g d\ell = \frac{1}{3N}\tilde{g}_{ii}d\ell$, $\Omega_{\tilde{g}} d\ell = \frac{1}{3N}g_{i\neq j}d\ell$, and $\tilde{\Omega}_{\tilde{g}} d\ell = \frac{1}{6N}\tilde{g}_{i\neq j}d\ell$, where

$$g_{ij} d\ell = g^2\int_{\vec{q}}^{>} D(\vec{q})\mathbf{G}_i(\vec{q})\boldsymbol{\tau}_z\mathbf{G}_j(\vec{q})\boldsymbol{\tau}_z \tag{D1}$$

$$\tilde{g}_{ij} d\ell = \tilde{g}^2\int_{\vec{q}}^{>}\tilde{D}(\vec{q})\mathbf{G}_i(\vec{q})\boldsymbol{\tau}_z\mathbf{G}_j(\vec{q})\boldsymbol{\tau}_z. \tag{D2}$$

Using that

$$\mathbf{G}_i(\vec{q})\boldsymbol{\tau}_z\mathbf{G}_j(\vec{q})\boldsymbol{\tau}_z = -\frac{1}{\vec{q}^2}\left[1-(1-\cos\beta_{ij})\frac{\mathbf{q}^2}{\vec{q}^2}\right] + \text{terms that vanish under int.}, \tag{D3}$$

where $\cos\beta_{ij} = \hat{\mathbf{n}}_i \cdot \hat{\mathbf{n}}_j$, we can use the spherical symmetry of $D(\vec{q})$ to compute $g_{ij}d\ell$,

$$g_{ij}d\ell = -8\int_{\vec{q}}^{>} \frac{1}{|\vec{q}|^3}\left[1 - \frac{2}{3}(1-\cos\beta_{ij})\right] = -\frac{4}{\pi}^2\left[1 - \frac{2}{3}(1-\cos\beta_{ij})\right]d\ell. \tag{D4}$$

Using that $\cos\beta_{ii} = 1$ and $\cos\beta_{i\neq j} = 1/2$, this results in the expressions in Eqs. (33) and (35) for $\Omega_g d\ell$ and $\Omega_{\tilde{g}} d\ell$. For the integrals involving $\tilde{D}(\vec{q})$, we obtain

$$\begin{aligned}\tilde{g}_{ij}d\ell &= -32\int_{\vec{q}}^{>} \frac{1}{|\vec{q}|^3}\frac{1-(1-\cos\beta_{ij})\frac{\mathbf{q}^2}{\vec{q}^2}}{1-\frac{1}{6}\frac{\mathbf{q}^2}{\vec{q}^2}} \\ &= -\frac{8}{\pi^2}d\ell\int_0^{\pi} d\theta\sin\theta\frac{1-(1-\cos\beta_{ij})\sin^2\theta}{1-\frac{1}{6}\sin^2\theta} \\ &= -\frac{8}{\pi^2}d\ell\begin{cases}12\kappa & (i=j)\\ 6(1-4\kappa) & (i\neq j)\end{cases},\end{aligned} \tag{D5}$$

which reproduces Eqs. (34) and (36) for $\tilde{\Omega}_g d\ell$ and $\tilde{\Omega}_{\tilde{g}} d\ell$.

[1] A. Kitaev, Anyons in an exactly solved model and beyond, Ann. Phys. **321**, 2 (2006).

[2] G. Jackeli and G. Khaliullin, Mott insulators in the strong spin-orbit coupling limit: From Heisenberg to a quantum compass and Kitaev models, Phys. Rev. Lett. **102**, 017205 (2009).

[3] T. Takayama, A. Kato, R. Dinnebier, J. Nuss, H. Kono, L. S. I. Veiga, G. Fabbris, D. Haskel, and H. Takagi, Hyperhoneycomb iridate β-Li_2IrO_3 as a platform for Kitaev magnetism, Phys. Rev. Lett. **114**, 077202 (2015).

[4] S. K. Choi, R. Coldea, A. N. Kolmogorov, T. Lancaster, I. I. Mazin, S. J. Blundell, P. G. Radaelli, Y. Singh, P. Gegenwart, K. R. Choi, *et al.*, Spin waves and revised crystal structure of honeycomb iridate Na_2IrO_3, Phys. Rev. Lett. **108**, 127204 (2012).

[5] S. Hwan Chun, J.-W. Kim, J. Kim, H. Zheng, C. C. Stoumpos, C. D. Malliakas, J. F. Mitchell, K. Mehlawat, Y. Singh, Y. Choi, *et al.*, Direct evidence for dominant bond-directional interactions in a honeycomb lattice iridate Na_2IrO_3, Nat. Phys. **11**, 462 (2015).

[6] P. Warzanowski, N. Borgwardt, K. Hopfer, J. Attig, T. C. Koethe, P. Becker, V. Tsurkan, A. Loidl, M. Hermanns, P. H. M. van Loosdrecht, *et al.*, Multiple spin-orbit excitons and the electronic structure of α-$RuCl_3$, Phys. Rev. Res. **2**, 042007(R) (2020).

[7] K. W. Plumb, J. P. Clancy, L. J. Sandilands, V. V. Shankar, Y. F. Hu, K. S. Burch, H.-Y. Kee, and Y.-J. Kim, α-$RuCl_3$: A spin-orbit assisted Mott insulator on a honeycomb lattice, Phys. Rev. B **90**, 041112(R) (2014).

[8] X.-G. Zhou, H. Li, Y. H. Matsuda, A. Matsuo, W. Li, N. Kurita, G. Su, K. Kindo, and H. Tanaka, Possible intermediate quantum spin liquid phase in α-$RuCl_3$ under high magnetic fields up to 100 T, Nat. Commun. **14**, 5613 (2023).

[9] H. Suzuki, H. Liu, J. Bertinshaw, K. Ueda, H. Kim, S. Laha, D. Weber, Z. Yang, L. Wang, H. Takahashi, *et al.*, Proximate ferromagnetic state in the Kitaev model material α-$RuCl_3$, Nat. Commun. **12**, 4512 (2021).

[10] X. Liu, T. Berlijn, W.-G. Yin, W. Ku, A. Tsvelik, Y.-J. Kim, H. Gretarsson, Y. Singh, P. Gegenwart, and J. P. Hill, Long-range magnetic ordering in Na_2IrO_3, Phys. Rev. B **83**, 220403(R) (2011).

[11] F. Ye, S. Chi, H. Cao, B. C. Chakoumakos, J. A. Fernandez-Baca, R. Custelcean, T. F. Qi, O. B. Korneta, and G. Cao, Direct evidence of a zigzag spin-chain structure in the honeycomb lattice: A neutron and x-ray diffraction investigation of single-crystal Na_2IrO_3, Phys. Rev. B **85**, 180403(R) (2012).

[12] J. A. Sears, Y. Zhao, Z. Xu, J. W. Lynn, and Y.-J. Kim, Phase diagram of α-$RuCl_3$ in an in-plane magnetic field, Phys. Rev. B **95**, 180411(R) (2017).

[13] A. U. B. Wolter, L. T. Corredor, L. Janssen, K. Nenkov, S. Schönecker, S.-H. Do, K.-Y. Choi, R. Albrecht, J. Hunger, T. Doert, *et al.*, Field-induced quantum criticality in the Kitaev system α-$RuCl_3$, Phys. Rev. B **96**, 041405(R) (2017).

[14] Y.-F. Jiang, T. P. Devereaux, and H.-C. Jiang, Field-induced quantum spin liquid in the Kitaev-Heisenberg model and its relation to α-$RuCl_3$, Phys. Rev. B **100**, 165123 (2019).

[15] S. Pradhan, N. D. Patel, and N. Trivedi, Two-magnon bound states in the Kitaev model in a [111] field, Phys. Rev. B **101**, 180401(R) (2020).

[16] C. Hickey and S. Trebst, Emergence of a field-driven $U(1)$ spin liquid in the Kitaev honeycomb model, Nat. Commun. **10**, 530 (2019).

[17] F. Yılmaz, A. P. Kampf, and S. K. Yip, Phase diagrams of Kitaev models for arbitrary magnetic field orientations, Phys. Rev. Res. **4**, 043024 (2022).

[18] A. Ralko and J. Merino, Novel chiral quantum spin liquids in Kitaev magnets, Phys. Rev. Lett. **124**, 217203 (2020).

[19] S.-S. Zhang, G. B. Halász, and C. D. Batista, Theory of the Kitaev model in a [111] magnetic field, Nat. Commun. **13**, 399 (2022).

[20] M. Gohlke, R. Moessner, and F. Pollmann, Dynamical and topological properties of the Kitaev model in a [111] magnetic field, Phys. Rev. B **98**, 014418 (2018).

[21] K. B. Yogendra, T. Das, and G. Baskaran, Emergent glassiness in the disorder-free Kitaev model: Density matrix renormalization group study on a one-dimensional ladder setting, Phys. Rev. B **108**, 165118 (2023).

[22] H. Nielsen and M. Ninomiya, Absence of neutrinos on a lattice: (I). Proof by homotopy theory, Nucl. Phys. B **185**, 20 (1981).

[23] H. Nielsen and M. Ninomiya, Absence of neutrinos on a lattice: (II). Intuitive topological proof, Nucl. Phys. B **193**, 173 (1981).

[24] H. Nielsen and M. Ninomiya, A no-go theorem for regularizing chiral fermions, Phys. Lett. B **105**, 219 (1981).

[25] H. Suzuki, A no-go theorem for the Majorana fermion on a lattice, Prog. Theor. Phys. **112**, 855 (2004).
[26] S. D. Drell, M. Weinstein, and S. Yankielowicz, Strong-coupling field theories. II. Fermions and gauge fields on a lattice, Phys. Rev. D **14**, 1627 (1976).
[27] T. C. Lang and A. M. Läuchli, Quantum Monte Carlo simulation of the chiral Heisenberg Gross-Neveu-Yukawa phase transition with a single Dirac cone, Phys. Rev. Lett. **123**, 137602 (2019).
[28] Y. D. Liao, X. Y. Xu, Z. Y. Meng, and Y. Qi, Caution on Gross-Neveu criticality with a single Dirac cone: Violation of locality and its consequence of unexpected finite-temperature transition, Phys. Rev. B **108**, 195112 (2023).
[29] B. H. Wellegehausen, D. Schmidt, and A. Wipf, Critical flavor number of the Thirring model in three dimensions, Phys. Rev. D **96**, 094504 (2017).
[30] Z. Wang, F. Assaad, and M. Ulybyshev, Validity of SLAC fermions for the $(1+1)$-dimensional helical Luttinger liquid, Phys. Rev. B **108**, 045105 (2023).
[31] K. G. Wilson, Confinement of quarks, Phys. Rev. D **10**, 2445 (1974).
[32] P. H. Ginsparg and K. G. Wilson, A remnant of chiral symmetry on the lattice, Phys. Rev. D **25**, 2649 (1982).
[33] D. B. Kaplan, A method for simulating chiral fermions on the lattice, Phys. Lett. B **288**, 342 (1992).
[34] R. Narayanan and H. Neuberger, A construction of lattice chiral gauge theories, Nucl. Phys. B **443**, 305 (1995).
[35] B. A. Bernevig, T. L. Hughes, and S.-C. Zhang, Quantum spin Hall effect and topological phase transition in HgTe quantum wells, Science **314**, 1757 (2006).
[36] X.-L. Qi, Y.-S. Wu, and S.-C. Zhang, Topological quantization of the spin Hall effect in two-dimensional paramagnetic semiconductors, Phys. Rev. B **74**, 085308 (2006).
[37] H. Hu and F. Krüger, Nature of topological phase transition of Kitaev quantum spin liquids, Phys. Rev. Lett. **133**, 146603 (2024).
[38] H. Isobe, B.-J. Yang, A. Chubukov, J. Schmalian, and N. Nagaosa, Emergent non-Fermi-liquid at the quantum critical point of a topological phase transition in two dimensions, Phys. Rev. Lett. **116**, 076803 (2016).
[39] M. D. Uryszek, F. Krüger, and E. Christou, Fermionic criticality of anisotropic nodal point semimetals away from the upper critical dimension: Exact exponents to leading order in $\frac{1}{N_f}$, Phys. Rev. Res. **2**, 043265 (2020).
[40] A. N. Vasil'ev, S. É. Derkachev, N. A. Kivel', and A. S. Stepanenko, The $1/n$ expansion in the Gross-Neveu model: Conformal bootstrap calculation of the index η in order $1/n^3$, Theor. Math. Phys. **94**, 127 (1993).
[41] J. Gracey, Calculation of the exponent η to $O(1/N^2)$ in the $O(N)$ Gross Neveu model, Int. J. Mod. Phys. A **06**, 395 (1991).
[42] J. Gracey, Anomalous mass dimension at $O(1/N^2)$ in the $O(N)$ Gross-Neveu model, Phys. Lett. B **297**, 293 (1992).
[43] J. Gracey, Computation of critical exponent η at $O(1/N^3)$ in the four-fermion model in arbitrary dimension, Int. J. Mod. Phys. A **09**, 727 (1994).